From linear stability analysis to three-dimensional organisation in an incompressible open cavity flow

Luc Pastur, Yann Fraigneau, François Lusseyran, Jérémy Basley

From linear stability analysis to three-dimensional organisation in an incompressible open cavity flow

L.R. Pastur[1,2] and Y. Fraigneau[2] and F. Lusseyran[2] and J. Basley[1,2,3]

[1] *Université Paris Sud 11, F-91405 Orsay Cedex, France*
[2] *LIMSI-CNRS BP 133, F-91403 Orsay Cedex, France*
[3] *Laboratory For Turbulence Research in Aerospace and Combustion, Department of Mechanical and Aerospace Engineering, Monash University, Clayton 3800, Australia*

PACS 47.10.ad – Navier-Stokes equations
PACS 47.11.Df – Finite volume methods
PACS 47.15.Rq – Laminar flows in cavities, channels, ducts, and conduits
PACS 47.20.Qr – Centrifugal instabilities

Abstract – Three-dimensional direct numerical simulations of an incompressible open square cavity flow are conducted. Features of the permanent (non-linear) regime together with the linear stability analysis of a two-dimensional steady base flow are discussed. Spanwise boundary conditions are periodic and control parameters set such that the shear layer is stable with respect to Kelvin-Helmholtz modes. Three branches of destabilising modes are found. The most destabilising branch is associated with steady modes, over a finite range of spanwise wavenumbers. The two other branches provide unsteady modes. Features of each branches are recovered in the permanent regime: wavelength of the most powerful spanwise Fourier mode, swaying phenomenon, angular frequencies, indicating that modes of each branches are selected and interact in the permanent flow.

Introduction. – Open cavity flows belong to the family of impinging flows, which are known to develop self-sustained oscillations. For decades, an extensive literature has been devoted to the study of such flows [?, ?, ?, ?, ?, ?, ?, ?, ?, ?, ?, ?, ?, ?]. The main features of open cavity flows, in the incompressible limit, may be roughly summarized as follows. The shear layer that forms between the outer and inner flows is known to be unstable with respect to streamwise Kelvin-Helmholtz modes, beyond some critical value of the Reynolds number. Kelvin-Helmholtz modes develop, downstream in the shear layer, from perturbations initiated at the upward corner. The unstable shear layer rolls up on itself to produce vortices that cyclically collide with the downward edge. Changes in the pressure field at impingement are instantaneously fed back to the upward edge, due to incompressibility or, equivalently, when the cavity length is small in regard to the acoustic wavelength and the material velocity small before sound celerity. Feedback then initiates the growth of a new perturbation at the upward edge. Therefore, both upward and downward edges are locked in phase, giving rise to strong self-sustained oscillations, whose frequency both depends on the incoming flow velocity, the cavity length, and the boundary layer thickness at the upward edge.

What has been far less studied is the cavity inner-flow, which exhibits non-trivial three-dimensional organisation [?, ?, ?, ?]. Centrifugal instabilities were shown to give rise to Taylor-Görtler-like rolls beyond a critical Reynolds number [?, ?]. The main inner-flow recirculation bends the pathline of material particles, which are subject to inertial forces. When viscous terms cannot overcome centrifugal effects, instabilities may develop, eventually giving rise to the formation of stable raw of pairs of counter-rotating vortices, in the spanwise direction, as observed in experiments or direct numerical simulations of the flow [?, ?, ?]. Recently, numerical studies have been carried out in unsteady cavity flows driven by Kelvin-Helmholtz instabilities, in compressible [?] and incompressible [?] regimes.

Our present contribution relies on a detailed analysis of intrinsic features of the inner flow, in an open cavity flow at a Reynolds number below the threshold of Kelvin-Helmholtz instability. Three-dimensional direct numerical simulations of the cavity flow are conducted with peri-

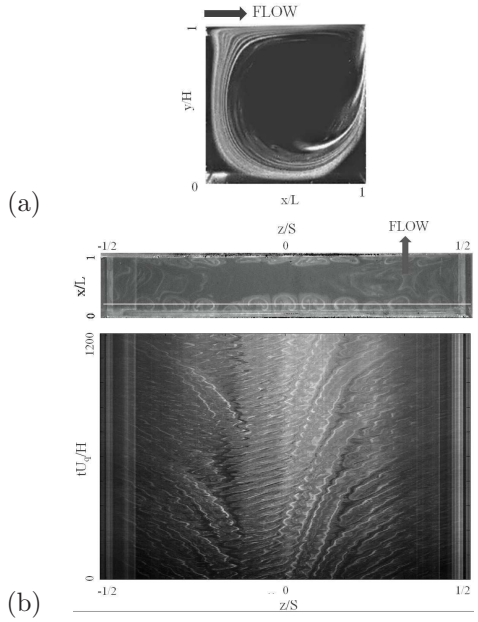

Fig. 1: Top: spanwise topview of the flow. Bottom: space-time diagram of the Taylor-Görtler rolls dynamics. The space-time diagram is made of the vertical concatenation of the spatial line shown in the top picture (the line intercepts the mushroom-like structure, close to the cavity upstream wall). From an experimental cavity flow, at $\Gamma_L = 1$, $Re_H \simeq 5\,800$.

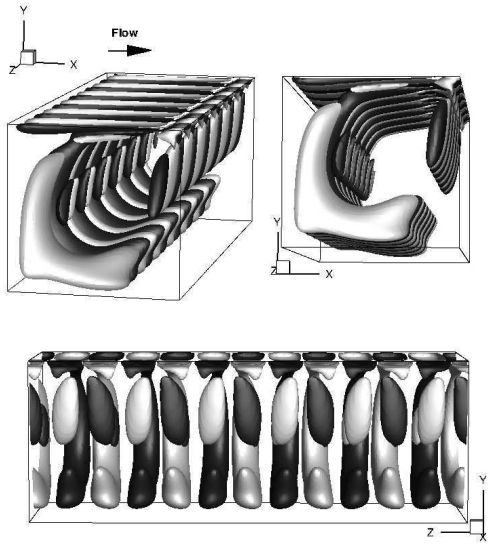

Fig. 2: Three views of Taylor-Görtler structure, as isosurfaces of dimensionless helicity hU_q^2/H (edge values ± 5.8). Only one half of the spanwise direction is represented for the sake of clarity. Spanwise boundary conditions are periodic. Top pictures are side-views of the structure, slightly seen from above and downstream (flow direction is indicated by the arrow). Bottom picture is a front view from the cavity downstream wall. Black corresponds to negative values of helicity, white to positive values.

odic spanwise boundary conditions, in order to get rid of border effects. A linear stability analysis is conducted, on a two-dimensional steady state with respect to three-dimensional perturbations. As it will be shown, three branches of (spanwise) growing modes are found, whose features are recovered in the permanent regime with little distortion, though coupled through non-linear terms.

Cavity flow features. – Instabilities in the shear layer primarily depend on the dimensionless cavity length $\Gamma_{\theta_0} = L/\theta_0$, ratio of cavity length, L, to boundary layer momentum thickness, θ_0, at the upward edge, the Reynolds number Re$=U_0 L/\nu$, based on L and incoming velocity, U_0, at the upstream cavity wall, and, for a lower part, the cross-stream aspect ratio $\Gamma_L = L/H$, defined as the ratio of cavity length, L, to cavity height, H.

The curvature induced by the main flow recirculation, inside the cavity, shown in fig **??**a, is responsible for the development of centrifugal instabilities, over some range of the control parameters. Relevant parameters, there, are the Reynolds number based on cavity height, $Re_H = U_0 H/\nu$, Γ_L and H/θ_0 [**?**]. In the non-linear saturated regime, centrifugal instabilities give rise to spanwise alley of pairs of counter-rotating vortices, as shown in the spanwise cut (top view) of fig **??**b (top). Each pair wraps the main inner-flow recirculation, forming torus-like patterns with major axis in the streamwise plane [**?**, **?**]. As shown in [**?**], spanwise walls, at $z/S = \pm 1/2$ where S is the span, generate a Bödewadt pumping, responsible, at $\Gamma_L = 1$, for a drift of the Taylor-Görtler rolls toward one wall or the other, as can be seen in the experimental space-time diagram of fig **??**b (bottom). In this figure, oblique lines correspond to drifting structures, and it is clear, from the different slopes, that inner spanwise dynamics is associated with several drift velocities, depending on the spanwise position, z. Henceforth, drift motions introduce additional unsteadiness in the flow, enriching the low-frequency range of power spectra.

Direct numerical simulations. – In order to get the intrinsic features of the inner flow, a three-dimensional direct numerical simulation is performed with periodic spanwise boundary conditions.

Numerical methods. The study addresses an incompressible and isothermal flow whose governing equation can be described by the non-dimensional Navier-Stokes equations:

$$\left\{ \begin{array}{rcl} \dfrac{\partial \boldsymbol{U}}{\partial t} + (\boldsymbol{U}\cdot\nabla)\,\boldsymbol{U} & = & -\nabla P + \dfrac{1}{Re}\Delta \boldsymbol{U} \\ \nabla\cdot\boldsymbol{U} & = & 0 \end{array} \right. \qquad (1)$$

where $\boldsymbol{U}$ is the velocity field and P the pressure field. Numerical simulations are performed with the OLORIN code based on an incremental prediction – projection method [**?**]. Momentum equations are discretised with a finite volume approach on a staggered structured grid. The spatial discretisation of fluxes is carried out with a second-order

Fig. 3: Streamlines stem from a spanwise line, at the bottom of the cavity, close to the upstream wall (the seeding line is materialised in pictures). (a) Downstream half topview, (b) topview. Inlet flow is oriented along x. Trajectories forward in time form inner loops (gray in (a)), trajectories backward in time form larger loops (black in (b)). Isosurfaces of fig **??** are shown in transparency. One hundred particles seed the flow.

centred scheme in a conservative form and time derivation is approximated by a second-order backward differentiation formula. Viscous terms are implicitly evaluated whereas convective fluxes are explicitly estimated at time t^{n+1} by means of a linear Adams-Bashford extrapolation. The discretised form of the Navier-Stokes equations yields a Helmholtz-type problem of the form:

$$\left\{ \begin{array}{rcl} \left(I - \dfrac{2\Delta t}{3Re}\nabla^2\right)\boldsymbol{U}^{n+1} & = & -\nabla P^{n+1} + S^{n,n-1} \\ \nabla \cdot \boldsymbol{U}^{n+1} & = & 0 \end{array} \right. \quad (2)$$

where superscript n tags time t_n, Δt is the time step and $S^{n,n-1}$ is the source term gathering all explicit quantities, evaluated at times t_n and t_{n-1}. The integration is performed with an ADI (Alternating Direction Implicit) method [**?**]. The resulting velocity field $\boldsymbol{U}^*$ is not yet divergence-free. Incompressibility is imposed by using an incremental projection method [**?**]. The projection step requires to resolve a Poisson-type equation, using a relaxed Gauss-Seidel method coupled to a multigrid method, in order to accelerate convergence, where the source term relies on non-zero divergence of the predicted velocity field:

$$\nabla^2\phi = \nabla \cdot \boldsymbol{U}^* \quad (3)$$

where $\nabla\phi$ is the correction term. The Poisson equation is commonly solved with Neumann-type boundary conditions, where the normal derivative on the domain limits is zero. By doing so, the boundary condition, on the corresponding normal velocity component, is not affected by the correction term.

Numerical simulation setup. The geometric setup consists in an open cavity capped with a parallelepipedic duct in which is generated the channel flow driving the inner cavity flow. A cartesian coordinate system (x, y, z), for streamwise, crosswise and spanwise directions, respectively, is set midspan at the top of the upstream cavity wall. The cavity dimensions are $L = 5$ cm, $L/H = 1$, $S/H = 6$ (span over height). Upstream and downstream lengths of the duct are respectively $L_u/L = 1$ and $L_d/L = 3$ and its height is $H_v/H = 3$. The Reynolds number is set to $Re = 3\,850$ (bulk velocity $U_q = 1.2$ m/s), and the boundary layer momentum thickness is $\theta_0/H = 26\times10^{-3}$.

The total domain is meshed on $160 \times 128 \times 192$ nodes, among which $64 \times 64 \times 192$ are devoted to the cavity. The mesh, regular in the spanwise direction, is particularly refined close to the walls and at the cavity top plane in order to enhance the spatial resolution of boundary layers and shear-layer.

The inlet flow is determined by Dirichlet boundary conditions. The inlet velocity profile is preliminary calculated by means of a 2D simulation of a laminar channel flow in spatial development, representative of the experimental upstream vein. The profile is then extracted out of the appropriate cross-section of the channel-flow and extruded in the periodic spanwise direction. Usual non-sliding conditions are applied at the walls. The numerical simulation is carried out over a time-duration of 60 s (1440 time-units H/U_q), after overtaking the numerical transitory state of the flow.

Intrinsic features of Taylor-Görtler-like vortices. Raw of Taylor-Görtler-like vortical structures take place inside the cavity flow and wind around the main recirculation vortex, as shown in fig **??**. However, contrary to the wall-bounded configuration, no spanwise drift of the structure towards the spanwise walls is observed. Although the flow is not fully steady, it is insightful to consider streamlines released backward and forward to a seeding line at the upstream bottom quadrant of the cavity (materialized line in fig **??**), and consider streamlines as approximate material trajectories. Trajectories gather into beams and draw funnel-like shapes, materializing the coherent structures highlighted by iso-surfaces of helicity (see fig **??**). In addition, although particles may start aligned in the spanwise direction z, their trajectories coil around each other, which reveals an helical flow in Taylor-Götler vortices. There is no mass flux between two adjacent counter-rotating vortices. The only spanwise transfer occurs inside both corner vortices, at the bottom of the cavity. Particles seeded inside the core of the main recirculation describe concentric circles, characteristic of a solid rotation (not shown in the

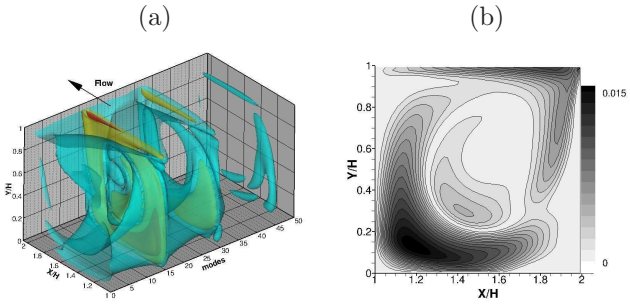

Fig. 4: (a) Each (x, y) slice represents the power structure, in the (x, y) plane, of spanwise Fourier modes $e^{ik_m z}$ from a discrete Fourier decomposition of the permanent flow, where $k_m = 2\pi m/S$ is the m^{th} mode wave-vector. Slices of fifty modes are shown and connected by isosurfaces with values $1.2u_x/U_q = 10^{-4}$ (blue), 10^{-3} (yellow), 10^{-2} (red). Most energetic modes are found for $m = 15$ and $m = 30$ (red colors). (b) Streamwise structure of the most energetic spanwise Fourier mode, $m = 15$. Colorscale encodes power spectral density of u_x, in units of U_q.

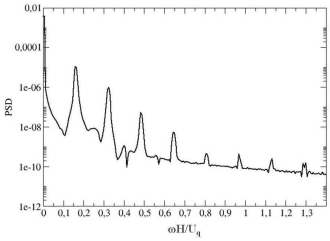

Fig. 5: Power spectral density computed from velocity time-recording at a probe inside the cavity.

figure).

A spectral Fourier analysis on velocity components, in the spanwise direction, yields another insight on the spatial arrangement of the flow (see fig **??**a). The most energetic Fourier modes, in space, are found for spanwise wavelengths, $\lambda/H \simeq 0.42$ ($\lambda/S \simeq 0.07$) and 0.84 ($\lambda/S \simeq 0.14$). Wavelength $\lambda/H = 0.42$ is therefore associated with the rake of vortex pairs, while its second harmonic, $\lambda/H = 0.84$, is connected to single vortices inside pairs. The streamwise (x, y) structure of the most energetic mode is shown in fig **??**b.

Spectral Fourier analysis on temporal samplings of velocity, at probes set in the cavity, shows that the flow is not quite stationary and contains a slight oscillating component, see fig **??**. This oscillation, found all over the cavity, is characterized by a angular frequency, $\omega H/U_q = 0.16$. A flow inspection reveals that this oscillating mode is associated with a swaying motion of Taylor-Görtler-rolls, around the main recirculation. In fig **??**, the slightly swaying motion is mainly observed on the inner blobs of helicity, close to the upstream cavity wall (better seen on the top right picture).

It is worthwhile noticing that the mode with largest growth-rate found in [**?**], for $\Gamma_L = 1$ and Mach numbers $M > 0.3$ has a wavenumber $\lambda/H \simeq 0.5$, similar to our $\lambda/H = 0.42$. This mode, in [**?**], is expected to be a steady mode ($\omega = 0$). In our configuration, the non-linearly saturated regime is found slightly unsteady, with $\omega H/U_q = 0.16$. This discrepancy motivates a three-dimensional linear stability analysis of the flow in the incompressible limit ($M = 0$).

Linear stability analysis. – Stability properties of a two-dimensional steady base state, with respect to spanwise perturbations, are now considered.

Principle. The method is described in [**?**]. This is aimed at characterizing the time-evolution of infinitesimal perturbations, $\boldsymbol{u}'$, with respect to an unstable steady base flow, $\boldsymbol{U}_0$, by means of linearised Navier-Stokes equations. In compact form, the system rewrites:

$$\frac{\partial \boldsymbol{u}'}{\partial t} = N_U \boldsymbol{u}' + D\boldsymbol{u}' \equiv A\boldsymbol{u}', \tag{4}$$

where N_U is the linearised operator of evolution associated with the eulerian part of the Navier-Stokes equations and D is the linear operator associated with viscous terms. The main instability features are depicted by the leading eigenpairs of the linear evolution operator, A, namely eigenpairs with the greatest real part. Leading eigenpairs are determined by the Arnoldi method.

Choice of the base flow and initial perturbation form. A preliminary two-dimensional numerical simulation, in the streamwise plane (x, y), for the same Reynolds number, $Re = 3\,850$, exhibits a stable steady-state flow, $\boldsymbol{U}_0^{2D}$. As a consequence, in the three-dimensional configuration under study, the instability of the base-flow must occur with respect to spanwise modes, as it is observed in three-dimensional numerical simulations of the Navier-Stokes equations (**??**). Therefore, the two-dimensional base-flow, $\boldsymbol{U}_0^{2D}$, is perturbated with initial conditions of the form:

$$\boldsymbol{u}'(x, y, z) = \boldsymbol{u}_0(x, y) \exp\left(i\frac{2\pi}{\lambda_j} z\right) \exp\left(\mu_j t\right), \tag{5}$$

that is, a mode of wavelength $\lambda_j = L/m$, $m \in \mathbb{N}^\star$, in the spanwise direction, and (complex) growth-rate $\mu_j = \sigma_j + i\omega_j$, with σ_j the temporal growth-rate and ω_j the angular frequency. Only stationary wave-like modes are considered since no spanwise drift is expected in the permanent flow.

Linearly growing modes. The base flow loses stability with respect to modes with positive growth-rate, $\sigma > 0$. Three branches of linearly growing modes are found, whose temporal growth-rate σ and angular frequency ω, as functions of λ, are illustrated in fig **??**. Modes with positive growth-rates have wavelength in the range $[0.24H, 1.32H]$, confirming the base-flow stability with respect to streawise perturbations (vanishing wavenumbers).

One branch (black squares) is associated with a stationary bifurcation ($\omega = 0$), on the wavelength range

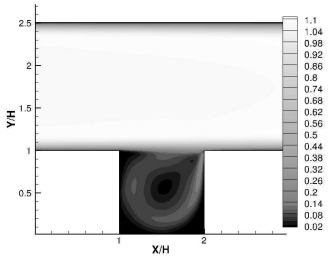

Fig. 6: Two-dimensional steady base-flow, solution of equations (**??**) for $Re = 3\,850$ and $\Gamma_L = 1$.

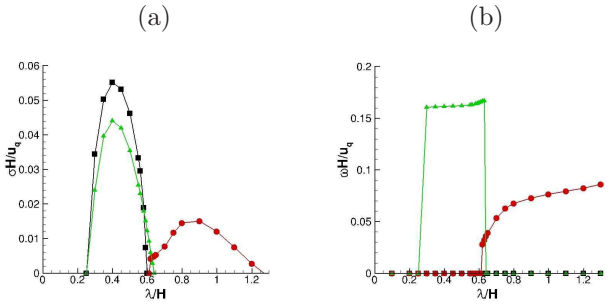

Fig. 7: Dimensionless growth-rate (a) and angular frequency (b) with respect to dimensionless spanwise wavenumber λ/H. Three families are found: *i)* steady growing modes (black squares), *ii)* oscillatory growing modes, with a constant angular frequency, $\omega H/U_q \simeq 0.16$, and small wavelength, $\lambda/H < 0.62$ (green triangles), *iii)* oscillatory growing modes of larger wavelength, with an angular frequency increasing with wavelength (red circles). Mode with the highest growth-rate belongs to family *i)* with a dimensionless wavelength $\lambda/H \simeq 0.4$.

$\lambda/H \in [0.24, 0.618]$. The largest growth-rate on this branch is found at $\lambda/H = 0.402$, close to the wavelength found for the raw of Taylor-Görtler-like vortices ($\lambda_{TG}/H \simeq 0.42$). We will refer to this mode as mode (i). A spatial representation of mode (i) is shown in fig **??**.

In fig **??** is also found, over the range of wavelength $\lambda/H \in [0.24, 0.642]$, another branch of solutions (green triangles) with positive growth-rates, and angular frequencies roughly constant over the range, at $\omega_{ii}H/U_q = 0.16$, very close to the one of Taylor-Görtler-like vortices. For this branch, the highest growth-rate is found, again, for $\lambda/H \simeq 0.4$, and we will refer to this mode as mode (ii). A comparison of both real and imaginary parts of mode (ii), in fig **??**, reveals a swaying motion of the structure around the main recirculation.

When the growth-rate of the stationary branch crosses zero, at $\lambda/H = 0.618$, a new branch rises, on the range $\lambda/H \in [0.618, 1.32]$, characterized by a non-zero angular frequency (red circles). Following this oscillatory branch, the angular frequency increases from 0 to about $\omega H/U_q = 0.092$, with a linear variation beyond $\lambda/H = 0.78$. In this family, the mode with the largest growth-rate, referred to as mode (iii), is found for $\lambda_{iii}/H \simeq 0.82$ with $\omega_{iii}H/U_q \simeq 0.075$.

From instability to permanent flow. The inner flow most energetic structure, in the permanent flow, has both a spanwise wavelength, λ_{TG}/H, and a streamwise structure, in close accordance with those of mode (i), the most linearly unstable mode in our linear stability analysis (compare figs **??**b and **??**). However, mode (i) is steady, whereas the permanent regime exhibits a slightly unsteady swaying motion. Note that transient dynamics, although not fully excluded, are very unlikely, since simulations in the permanent flow cover a time-range of 1 440 time-units H/U_q. In fact, when considering the power spectral density of fig **??**, in the permanent regime, a main peak is found at $\omega_{TG}H/U_q \simeq 0.16$, which precisely is the angular frequency of modes of the second family. Moreover, the streamwise structure of mode (ii), in that family, exhibits a swaying-like motion, as shown in fig **??**, when comparing both real and imaginary parts. Such features suggest that this mode, as mode (i), is also selected by the flow. Note that linear modes are recovered in the permanent regime without significant distortion, despite of non-linear effects.

It is worth to note that the angular frequency of the third family mode, with the highest growth-rate, is $\omega_{iii}H/U_q \simeq 0.07$. Would such a mode be present in the flow, it could couple to mode (ii) and generate components at $(\omega_{ii} \pm \omega_{iii})H/U_q$, i.e. 0.09 and 0.23. In the power spectral density of fig **??**, a lobe is actually found around $\omega H/U_q \simeq 0.25$, suggesting a non-linear (quadratic) coupling of mode (iii) with mode (ii). In addition, the spanwise Fourier mode associated with $m = 30$, in fig **??** for the permanent regime, is not found in the linear stability analysis, indicating that this mode is rather generated by quadratic non-linear self-interaction of mode $m = 15$.

Conclusion. – Three dimensional direct numerical simulations of an open square cavity flow are performed in the incompressible limit and at Reynolds number $Re = 3\,850$, $L/H = 1$, below the threshold of shear layer instability. They reproduce most of the inner flow characteristic features observed in experiments. As a result of centrifugal instabilities, vortical structures develop and form spanwise alley of pairs of counter-rotating vortices [**?**, **?**]. When spanwise boundary conditions are periodic, the alley of vortices is fixed. However, in the non-linearly saturated regime, a closer inspection of the flow reveals a slightly swaying motion of the structure of vortices around the main recirculation flow.

The fastest (linearly) growing spanwise mode, in a linear stability analysis of the steady base state, has a wavelength $\lambda/H = 0.4$, fairly close to the wavelength associated with the spanwise alley of vortices. However, from stability analysis, this mode is expected stationary. Yet, the swaying motion is caught by a mode of the second family, whose growth-rate is maximal for wavelengths of the order of λ_{TG}. Surprisingly, streamwise structures, wavelength and

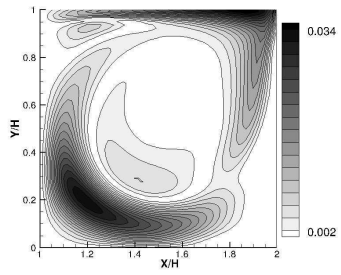

Fig. 8: Streamwise structure (modulus) of the spanwise mode with largest growth rate of the first family ($\omega = 0$), referred to as mode (i).

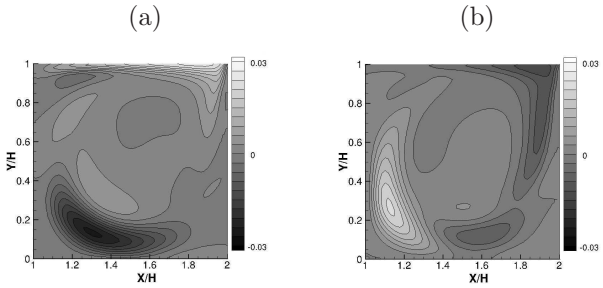

Fig. 9: Streamwise structure of the spanwise eigen-function with largest growth-rate of the second family ($\omega H/U_q = 0.16$), referred to as mode (ii): real part (a), imaginary part (b). The colorscale encodes u_x, in units of U_q.

angular frequencies of linear modes are not much distorted in the non-linear regime. Non-linear effects are revealed by coupling modes of two families, namely the modes with largest growth-rates from families (ii) and (iii).

Note that beyond the drift motion initiated by the pumping effect at the spanwise walls, a secondary bifurcation towards an unsteady oscillating phenomenon of the alley of vortices has been reported in experiments, see for instance [**?**]. Although the streakline features of this secondary instability could possibly be understood as the result of a swaying motion, it is not possible, yet, to ascertain whether both phenomenons, in simulations and experiments, be related or not.

* * *

This work has been supported by the ANR project CORMORED. J.B. gratefully acknowledges fruitful discussions with J. de Vicente Buendia. The authors wish to thank Th.M. Faure for fruitfull discussions.

REFERENCES

[1] Rossiter, J.E., *Aeronautical Research Council Reports and Memoranda* **3438** (1964).
[2] M. Gharib, A. Roshko, *Journal of Fluid Mechanics* **177** (1987) 501-530.
[3] W.R. Miksad, *Journal of Fluid Mechanics* **56** (1972) 695-719 .
[4] D. Rockwell, *Journal of Fluids Engineering* **99** (1977) 152-165.
[5] D. Rockwell, C. Knisely, *Journal of Fluid Mechanics* **93** (1979) 413-432.
[6] Rockwell, D. & Naudascher, E., *Annual Review of Fluid Mechanics* **11** (1979) 67-94.
[7] Knisely, C. & Rockwell, D., *Journal of Fluid Mechanics* **116** (1982) 157-186.
[8] W.R. Miksad, F.L. Jones, E.J. Powers, Y.C. Kim, L. Khadra, *Journal of Fluid Mechanics* **123** (1982) 1-29.
[9] Kegerise M, Spina E, Garg S, Cattafesta L (2004) *Physics of Fluids* **16** (2004) 678-687.
[10] L. R. Pastur, F. Lusseyran, T. M. Faure, Y. Fraigneau, R. Pethieu, P. Debesse, *Experiments in Fluids* **44** (4) (2008) 597-608 .
[11] N. Delprat, *Physics of Fluids* **18** (2006) 071703.
[12] Basley, J., Pastur, L. R., Lusseyran, F., Faure, Th. M. & Delprat, N., *Experiments in Fluids* **50** (2010) 905-918.
[13] B. Farkas, G. Paàl, G. Szabó, *Physics of Fluids* **24** (2012) 027102.
[14] Neary, N.D. & Stephanoff, K.D., *Physics of Fluids* **30** (1987) 2936-2946.
[15] Brès, G. A., & Colonius, T., *Journal of Fluid Mechanics* **599** (2008) 309 - 339.
[16] Faure, Th. M., Adrianos, P., Lusseyran, F. & Pastur, L. R., *Experiments in Fluids* **42** (2007) 169-184.
[17] Faure, Th. M., Pastur, L. R., Lusseyran, F., Fraigneau, Y. & Bisch, D., *Experiments in Fluids* **47** (2009) 395-410.
[18] F. Alizard, J.-Ch. Robinet and X. Gloerfelt, *Computers and Fluids* (2012), in revision.
[19] Gadoin, E., Le Quéré, P. & Daube, O., *IJNMF* **37** (2001) 175–208.
[20] Hirsch, C., A Wiley interscience publication, **1** (1987) Wiley & Sons.
[21] Guermond, J. L. , Minev, P. D., Shen J., *CMAME* **195** (2006) 6011–6045.
[22] Mamum, C. K. & Tuckerman, L. S. (1995), *Physics of Fluids* **7**, 80-91.